International Journal of Heat and Technology
Vol. 44, No. 2, April, 2026, pp. 888-900
Journal homepage: http://iieta.org/journals/ijht

Computational Fluid Dynamics Analysis of Heat Transfer Enhancement in Flat Plate Solar Air Heaters Using Inclined Wing Vortex Generators

Naema Motaer Abbas[1,2*], Kadhim Fadhil Nasir[2,3]

[1] Department of Power Engineering Techniques, AL-Mussaib Technical College, Al-Musayyib 51006, Iraq
[2] Al-Furat Al-Awsat Technical University, Najaf 54001, Iraq
[3] Department of Machines and Equipment, Babil 51001, Iraq

Corresponding Author Email: neama.motaer.tcm.24@student.atu.edu.iq

https://doi.org/10.18280/ijht.440238

Received: 31 August 2025
Revised: 10 December 2025
Accepted: 19 December 2025
Available online: 30 April 2026

Keywords:
solar air heater, vortex generators, numerical simulation, thermal performance factor, heat transfer

ABSTRACT

The inclusion of vortex generators (VGs) significantly enhanced heat transfer performance, with the rectangular wings producing Nusselt numbers up to 570% higher than the baseline case, although accompanied by friction factor penalties approximately 6–9 times greater than those of smooth ducts. Both VG geometries achieved a thermal performance factor (TPF) greater than unity, while the triangular wings attained a TPF of 2.0. The results confirm that passive flow modification using VGs can substantially improve solar air heater (SAH) performance, with triangular wing geometry offering the most favorable thermo-hydraulic balance.

1. INTRODUCTION

Flat plate solar air heaters (FPSAHs) are commonly employed in solar thermal applications such as space heating, crop drying, and industrial preheating [1, 2]. They are popular owing to their simple structure, low production cost, and effectiveness in utilizing solar energy [3, 4]. A standard FPSAH is characterized by an absorber plate, air duct, and transparent cover, in which the solar radiation is absorbed and transferred to the air under the plate [5, 6]. Despite the advantages of smooth-plate configurations, thermal efficiency remains low with low convective heat transfer. A steady thermal boundary layer forms on the absorber plate with the motion of the airflow, and this offers heat exchange resistance and reduces the thermal performance and outlet temperature of the air [7, 8]. While heat transfer may improve with increased velocity of the airflow, thermal losses and pressure drop are more significant and therefore net efficiency gains are affected [9, 10].

To address these limitations, various heat transfer enhancement techniques have been investigated. These methods are generally categorized as active, passive, or compound [11, 12]. Active techniques involve external energy input, while passive techniques rely on geometric modifications to the surface or flow channel to promote turbulence without additional power. Compound techniques integrate both approaches. Of the passive methods, fins, ribs, and vortex generators are widely used [13, 14]. Fins increase heat transfer area, ribs disrupt the boundary layer in order to promote turbulence, and vortex generators induce secondary flows in order to mix the near-wall and core flows. Vortex generators are very effective because they create longitudinal vortices, usually penetrating significantly into the main flow, and are continuously disturbing the thermal boundary layer and thus enhancing convective heat transfer [15, 16]. Geometry, inclination, and arrangement are very critical for vortex generators, and must optimize thermal gains over pressure drop penalties [17, 18].

Many studies have been performed to design different shapes, configurations and arrangements of VGs in solar air heaters for improving heat transfer rate and overall thermo-hydraulic performance as passive technique by different researchers based on various numerical simulations as well as experimental validation. For a solar air heater, Charoensin-O-larn and Lertnuwat [19] numerically studied the impact of right-trapezoidal winglet vortex generators in an upwind and downwind tailoring configuration. The additional effect of the upwind orientation was the increase in near-wall velocity and enhanced convection, which enabled higher Nusselt number (Nu), friction factor (f), and thermal enhancement factor by comparison with the downwind test section. Bezbaruah et al. [20] performed an experimental investigation accompanied by numerical simulations on solar air-heated workers with modified conical vortex generators in a staggered array. They investigated Re = 3500–16000, for relative pitch ratios (2.67–15), and height ratios (0.17–0.34) with the help of ANSYS Fluent 19.2. Results included a maximum thermal enhance of up to 257%, a THPPmax = 2.04 from the FE, and empirical correlations for Nu and f. A natural-convection solar air heater equipped with a flexible porous winglet vortex generator system was modelled using transient two-way fluid–structure interaction [15]. The porous design improved blockage (16.8% reduction), improved external flow (8.3% enhanced), and improved outlet temperature (135% increase in air temperature rise over the smooth configuration and 500% increase over the solid winglet and smooth duct arrangement). Lertnuwat [21] numerically analysed the number and placement of holes in rectangular winglet vortex generators for Re = 3000–20000. Maintaining constant blockage ratio, a single-hole design gave the highest average Nu, while nine holes yielded the lowest. Friction factor changes were minor, and large, organised vortices were most beneficial for heat transfer.

Hu et al. [22] experimentally examined one-eighth-sphere vortex generators, varying deflection angle, relative transverse pitch, relative longitudinal pitch, relative height, and Re. The optimal case ($\alpha = 180°$) achieved THPP ≈ 2.03, with Nu and f up to 2.45× and 1.96× higher than smooth ducts, and new correlations were developed. Duarte et al. [23] numerically investigated louvered-winglet longitudinal vortex generators in a channel-type solar air heater for Re = 5000 and 20000. Rectangular winglets with larger louver area ratio, higher flap angle, and greater aspect ratio in a common-flow-down arrangement maximized performance (thermal enhancement factor = 3.418) and reduced pressure loss when louvers pointed toward the adiabatic plate. Van Hap et al. [24] studied perforated circular-segment vortex generators via 3-D RNG k–ε simulations and experiments for Re = 6000–18000 and attack angles = 30–90°. The best performance (THPP ≈ 1.3) was at 30°, with staggered arrangements outperforming inline by factors of 1.72 for Nu and 1.88 for f. Lertnuwat [25] numerically explored hole position on trapezoidal winglet vortex generators for Re = 3000–20000. Placing a hole near the dead zone improved Nu and reduced momentum flux toward the winglet, lowering pressure drag.

Sari et al. [26] experimentally and numerically assessed a solar air collector with baffles and delta winglet vortex generators. Adding six baffles and three DWLVG pairs improved thermal efficiency from 13% to ~20% and exergy efficiency to 30.44%, with average gains of 7.4% (thermal) and 12% (exergy). Promvonge et al. [27] numerically examined punched delta-winglet (P-DW) vortex generators for Re = 4000–24000, varying relative pitch and hole size. Reducing both parameters increased Nu and f, with gains of up to 78.21× and 5.9× over smooth ducts. A flapped variant (F-DW) yielded the highest performance (≈2.16). Alnakeeb et al. [28] used 3-D simulations to study a corrugated absorber plate with rectangular, trapezoidal, and delta vortex generators for Re = 7000–25000. VGs enhanced heat transfer but increased pressure loss, with the best thermo-hydraulic performance (0.91) for rectangular VGs at Re = 7000, $\alpha = 30°$. Pramod et al. [29] combined Computational Fluid Dynamics (CFD) and experiments on semi-conical vortex generators in a triangular duct solar air heater over Re = 6000–21000. They developed Nu and f correlations (errors less than7%) and used Artificial Neural Network (ANN) with Bonobo Optimisation to find an optimal THPP = 1.74. Koolnapadol et al. [2] experimentally evaluated rectangular-wing vortex generators for Re = 5290 – 22700, varying α and pitch ratio. RWVGs increased Nu by up to 5.79× and f by up to 43.97× over smooth ducts, with the best thermal performance (1.95) at $\alpha = 30°$, PR = 1.5.

Vortex generators have been successfully utilized in solar air heaters, convincing benefits due to disruption of thermal boundary layer and secondary flows are created which further promote the transfer of heat. While previous work has looked at different shapes, orientations, and arrangement, nearly all report results for only a single geometry or compare multiple shapes under different operating or geometric conditions. However, the inclination angle is an important parameter that influences flow structure and thermal performance, which indicates a lack of comparative CFD investigations specifically investigating rectangular versus triangular wing vortex generators at a 45° angle inclination.

The current study is aimed to cover this gap via modeling in ANSYS Fluent for two designs of flat-plate solar air heater with rectangular and triangular wings respectively. For a range of Reynolds numbers, a comparative assessment is provided for outlet temperature, heat transfer coefficient, Nusselt number, friction factor and thermal performance factor (TPF), facilitating the comparison of geometric-specific performance trade-offs.

Inspired by the above literature, the current experiment aims to offer a more direct and controlled comparison of vortex-generator concepts in flat-plate solar air heaters (SAHs). Unlike previous studies, where each investigation focused on a single geometry or mode shape and comparisons among different shapes were conducted under non-identical operating or geometric conditions, the present work examines rectangular and triangular wing vortex generators attached at the same 45° angle, blockage ratio, and pitch positioning in an otherwise identical duct [22-24, 29]. The simulations are conducted over a physically realistic ranges of air velocities (1.5–4.5 m/s, Re ≈ 9.5 × 103 – 2.9 × 104) and absorbed solar fluxes (200–1000 W/m²), and the performance is reported in the context of both conventional metrics (outlet temperature, Nusselt number, friction factor) and the TPF as compared to a smooth-plate baseline. Together, these features highlight the peculiar novelty and contribution of the present work on the spectrum of research on solar air heater with vortex generators.

2. NUMERICAL METHODOLOGY

2.1 Physical model

This study presents a numerical investigation of three different configurations of the flat plate: Config. 0: Flat absorber plate (reference case); Config. I: Vortex Generators (VGs) Triangular (wing-type) inclined at 45° on Absorber plate; Config. II: Vortex Generators (VGs) Rectangular (wing-type) inclined at 45° on Absorber plate; All Absorber plates length L = 2.0 m, width w = 1.0 m with h = 20 mm height and b = 30 mm width in each VG in enhanced cases. In both VG configurations, the longitudinal and transverse pitches are the same to allow for a direct performance comparison. The overall geometry of the plate is illustrated in Figure 1, and the geometric parameters are summarized in Table 1. This case smooth plate has the same plate dimensions but vortex elements are not included.

2.2 Computational domain and boundary conditions

The size is the rectangular duct, which consist of the inlet section, an absorber section which contains the VGs, and an outlet section where there must be fully developed flow at the exit. Table 2 presents the boundary conditions for the simulations Velocity inlet was applied with velocity values imposed to obtain the Reynolds number. A pressure outlet with zero-gauge pressure was used at the outlet. A uniform incident solar heat flux was imposed at the top surface of the absorber plate, and it was assumed adiabatic and no-slip for the side and bottom walls. The surfaces of vortex generators were treated, also, as no-slip. Air was considered as the working fluid, modeled as an incompressible ideal gas, with its properties being evaluated at the film temperature, for each of the test cases.

2.3 Governing equations

The continuity, momentum and energy equations were solved as steady-state, three-dimensional, incompressible Reynolds-averaged Navier–Stokes (RANS) equations:

Continuity equation:

$$\rho\left(\nabla \vec{V}\right) = 0 \tag{1}$$

Momentum equation:

$$\rho\, \nabla\, \vec{V}^2 = -\nabla P + \mu \nabla^2 \vec{V} \tag{2}$$

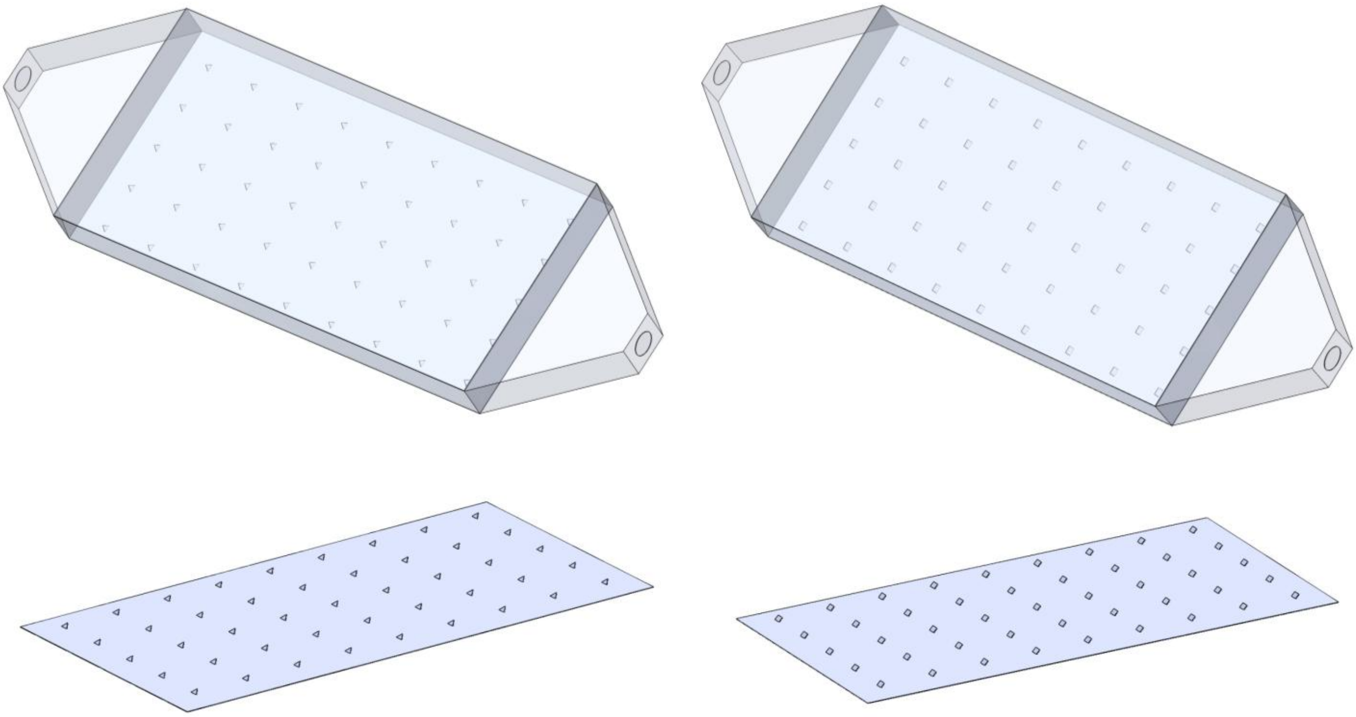

(a) Config. I

(b) Config. II

Figure 1. CAD geometry of (a) triangular and (b) rectangular vortex generator configurations

Table 1. Geometric parameters of absorber and vortex generators

Parameter	Symbol	Config. 0	Config. I	Config. II
Plate Length	L	2 m	2 m	2 m
Plate width	W	1 m	1 m	1 m
VG height	h	-	20 mm	20 mm
VG width	b	-	30 mm	30 mm
VG inclination	α	-	45°	45°
Longitudinal pitch	P_L	-	200 mm	200 mm
Transverse pitch	P_T	-	166 mm	166 mm
Rows × columns	$N_x \times N_y$	-	9 × 5	9 × 5
Arrangement	-	-	Inline	Inline

Table 2. Boundary conditions and solver setup

Domain region	Boundary type	Specification
Inlet	Velocity inlet	Uniform velocity (1.5, 3, 4.5 m/s) based on target Re, ambient temperature
Outlet	Pressure outlet	Gauge pressure = 0 Pa
Absorber plate	Wall, constant heat flux	Prescribed absorbed solar flux (200, 400, 600, 800, 1000 W/m^2)
Side walls	Adiabatic wall	No-slip, zero heat flux
Bottom wall	Adiabatic wall	No-slip, zero heat flux
Vortex generators	Wall	No-slip
Working fluid	Air	Properties at film temperature
Turbulence model	RNG k-ε	Enhanced wall treatment
Discretization	Second-order upwind	Momentum, energy, turbulence
Convergence	Residuals ≤ 10^{-6}	Energy residual ≤ 10^{-8}

Energy equation:

$$\rho C_P\left(\vec{\mathrm{V}}\,\nabla \mathrm{T}\right) = K\nabla^2 T \tag{3}$$

where, V is the velocity vector, ρ is the air density, $\vec{V}$ is the velocity vector, P is the pressure, T is the temperature, C_P is the specific heat, and K is the thermal conductivity.

The Reynolds number (Re) employed in defining the flow regime is:

$$Re = \frac{\rho\, u\, D_{eq}}{\mu} \tag{4}$$

where, ρ represents the fluid density, D_{eq} denotes the hydraulic diameter, u signifies the characteristic velocity, and μ indicates the dynamic viscosity. The hydraulic diameter is determined by:

$$D_{eq} = \frac{4\,A}{p_w} \tag{5}$$

where, A is the cross-sectional flow area and p_w is the wetted perimeter.

The RNG k−ε model with improved wall treatment was used for turbulence closure due to its proven capability of predicting separated and recirculating flows associated with VGs. All transport equations were solved with a second-order upwind scheme for accuracy of the solution.

2.4 Mesh generation and grid independence test

The computational meshes consisted of unstructured tetrahedron cells with local refinement around the VGs for capturing the flow separation and vortex structures. All solid surfaces were treated with prism inflation layers specifically so that the prisms could properly resolve the near-wall boundary layer.

An average Nusselt number (Nu) at the absorber plate was used as the grid independence criteria for Config. I as shown in Figure 2. For more than 4 × 10^{-6} elements, the changes in Nu were smaller than 0.1%, with further refinement. Thus, a mesh resolution with about 4 million elements was used for all cases (including the smooth plate configuration) to ensure comparability. Figure 3 depicts the final mesh for the triangular VG.

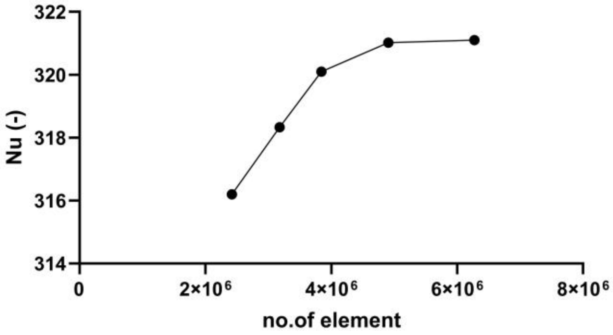

Figure 2. Grid independence test results for Config. I

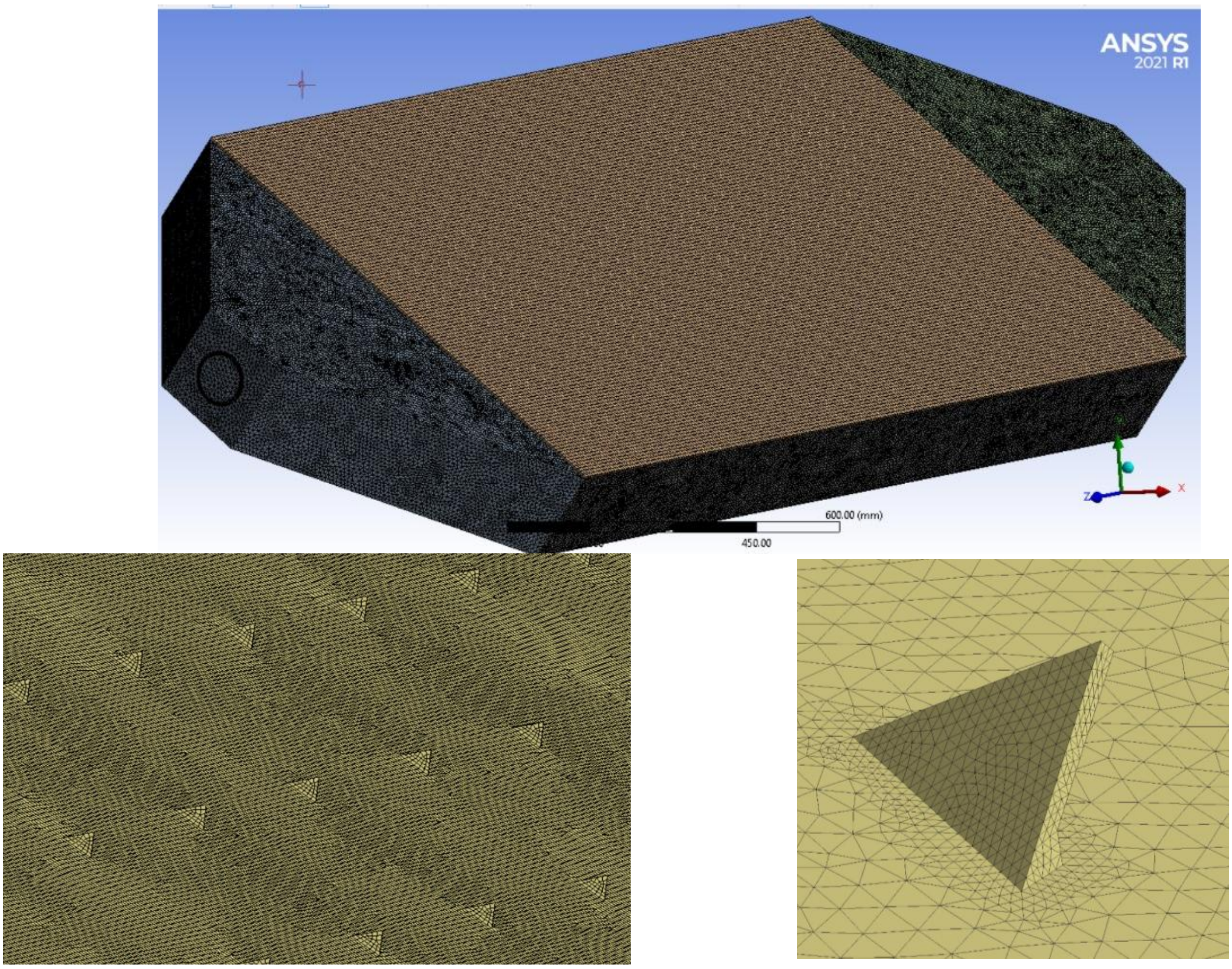

Figure 3. Computational mesh for the triangular vortex generator configuration

3. VALIDATION

Initially, the smooth plate setup (without vortex generators) was tested and validated with standard heat transfer and fluid flow correlations to verify the accuracy of the CFD model. This baseline case is selected as it has extensive documentation of its thermo-hydraulic characteristics in literature.

The Dittus–Boelter correlation is frequently used to predict the average Nusselt number for fully developed turbulent flow in a smooth rectangular duct:

$$Nu = 0.023\, Re^{0.8} Pr^{0.4} \tag{6}$$

where, Re is Reynolds number and Pr is the Prandtl number of air at the bulk temperature. For the broad range of investigated Reynolds numbers (Re = $9.5 \times 10^3 - 2.9 \times 10^4$) the Nusselt numbers predicted by the CFD were compared to the Dittus–Boelter correlation. The CFD results follow the correlation trend (Figure 4). Since entrance effects and the rectangular duct geometry tend to slightly elevate CFD predictions compared to those from the correlation at low Reynolds numbers, the results reach an almost identical value at high Reynolds numbers. The highest deviation between CFD and correlation has been less than ±8%, which is reasonable for turbulent heat transfer predictions. It establishes the suitability of the turbulence model and thermal boundary conditions applied on ANSYS Fluent for the problem.

Pressure drop characteristics were analyzed with the Darcy–Weisbach equation plus the Blasius correlation for smooth tubes with turbulent water flow:

$$f = 0.316\, Re^{-0.25} \tag{7}$$

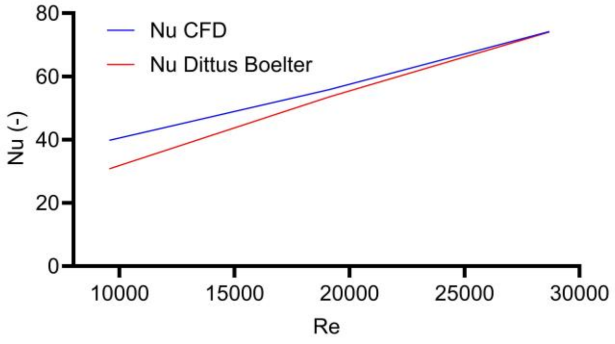

Figure 4. Validation of Computational Fluid Dynamics (CFD) and Dittus–Boelter correlation for Nusselt number

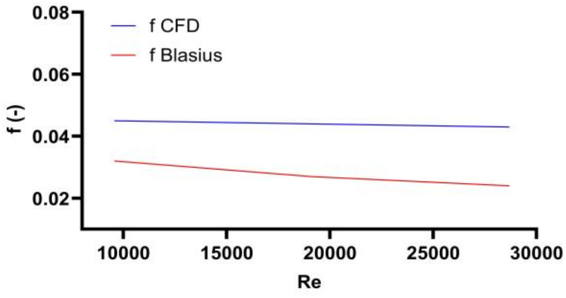

Figure 5. Validation of Computational Fluid Dynamics (CFD) and Blasius correlation for friction factor

The comparison drawn between the Blasius correlation and the CFD-predicted friction factors is shown in Figure 5. The CFD values consistently exceed the theoretical prediction by approximately 50–70%. The difference can be explained by short duct length, developing flow effects, and the geometry of this computational domain not being circular (the Blasius equation was valid for fully developed turbulent flow in circular tubes). In spite of this offset, the CFD results show the correct trend of decreasing with Reynolds number, and as such, the simulation study is validated.

The validation exercise shows that the CFD model was able to predict both thermal and hydraulic performance of a smooth plate solar air heater reasonably accurately. The near identical Nusselt number, which builds confidence in the thermal predictions compared to the Dittus Boelter correlation and the higher than ideal friction factor is qualitatively determined by the regional flow and geometrical development effects. As a result, this model can be confidently applied to test improved designs using the rectangular and triangular vortex generators.

4. RESULTS AND DISCUSSION

Figure 6 with respect to smooth duct (Config. 0), triangular configuration of vortex generators (Config. I), and rectangular arrangement vortex generators (Config. II) at airflow velocities of 1.5, 3, and also 4.5 m/s, shows the way the outlet air temperature changes with heat flux. In all cases, the outlet temperature is going up linearly with heat flux, which confirms that there exists a direct relation between the thermal reaction and the last solar input. For the smooth duct at 1.5 m/s, the exit temperature increased from 304.9 K at 200 W/m² to 331.6 K at 1000 W/m², a total increase of 27 K. Config. I and Config. The corresponding outlet temperatures obtained by II were 326 K and 335 K. This indicates that Config. Config set II generated airstream temperatures out of the outlet 3% higher than Config. I at low Reynolds numbers. The maximum outlet temperature for the smooth duct was 322.9 K (at 3 m/s) and 320 ℃ for Config. I and 323 K for Config. II. As residence time decreased with increasing velocity, the differences between configurations attenuated. At the 4.5 m/s, outlet temperatures decreased for all cases, with the smooth duct achieving values as low as 314.1 K, compared to Config. I and Config. II gave nearly identical values (314–315 K). In summary, the outlet temperature for the smooth duct was always the highest, and the vortex-generator configurations yielded the lowest outlet air temperatures; however, the latter was a relatively small difference. Nevertheless, this reduction is compensated with increased convective mixing and superior heat transfer coefficients which is a clear indication of the trade-off between bulk temperature rise and net heat transfer augmentation over wide range.

Figure 7 represents the dependence of Nusselt number (Nu) on heat flux for the smooth plate (Config. 0, Config. I and Config. II) and airflow velocities of 1.5, 3, and 4.5 m/s, respectively. Predicted Values of Nu increase with heat flux and with Reynolds number as a result of increasing intensity of heat transfer with convection. Nu values are also still low, 38 < Nu < 76 for the smooth plate, remaining true to a classical smooth-duct behavior. Conversely, thermal performance increases significantly with the introduction of vortex generators. At 1.5 m/s, Config. The maximum increment of Nu is from 48 for the smooth case to nearly 320–330 at high heat flux (a 570% improvement) in II. Similarly, Config. I attain Nu as high as 290, which is a 500% increase over that of the baseline. Config. At Nu boost both these at 4.5 m/s, efficiency (improves over Config. II attains 330 while Config. I reach 320, compared to smooth plate 77. The results indicate that vortex generators induce higher intensity secondary flows, better mixing, and thermal boundary layer disruption that led to significant enhancement of heat transfer. Config. Config. II (triangular vortex generators) is always better than Config. Such that I (rectangular), especially at low velocities where flow mixing is the dominant factor.

The enhanced surfaces' relative performance is measured in terms of the normalized Nusselt ratio (Nu/Nu_0) (Figure 8). At all Reynolds numbers and all heat fluxes, Nu/Nu_0 is greater than 4.0, reaffirming strong augmentation. Config. II at 1.5 m/s exhibits the best improvement, where $Nu/Nu_0 \approx 5.0$, representing a quintuple augmentation over the smooth plate. Config. I exhibit somewhat lower values ($Nu/Nu_0 \approx 4.1$–4.4), yet indicates strong intensification of the heat transfer. For higher velocities (3–4.5 m/s) turbulent mixing dominates forced convection at the smooth plate, and the enhancement thus decreases somewhat ($Nu/Nu_0 \approx 4.3$–4.5). Still, both configurations retain a healthy degree of lead with Config. II consistently outperforms Config. I by 6–10%.

Figure 9 illustrates the variation of the friction factor (f) with increasing heat flux for the three studied configurations at different flow velocities. For the smooth plate (Config. 0), the friction factor remained nearly constant across the range of heat fluxes, stabilizing at approximately $f \approx 0.045$. This confirms that in the absence of flow disturbance, pressure drop is mainly governed by velocity rather than heat flux. In contrast, the introduction of vortex generators in Config. I and Config. II led to significant increases in friction factor. At v = 1.5 m/s, Config. II exhibited the highest values, with f reaching 0.42 at 200 W/m^2, about 9 times higher than the smooth plate baseline. Config. I also showed enhanced friction, with $f \approx 0.38$ under the same condition, representing an increase of 8 times compared to Config. 0. At increased flow velocities (v = 3-4.5 m/s), the relative variation slightly decreased owing to the shorter residence time of air and greater inertial forces. At, e.g., v = 4.5 m/s and q = 1000 W/m^2, Config. II registered $f \approx 0.34$, whereas Config. I provided $f \approx 0.29$, still 7–8 times higher than the smooth plate. This trend verifies the fact that vortex generators are successful in increasing turbulence significantly, albeit at the expense of a substantially larger pressure drop, especially at lower velocities.

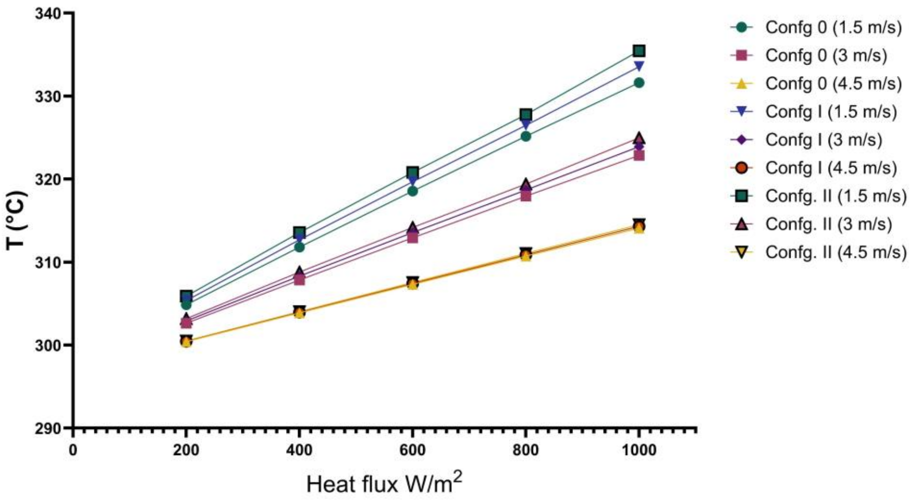

Figure 6. Variation of outlet air temperature with heat flux for smooth plate (Config. 0), triangular vortex generators (Config. I), and rectangular vortex generators (Config. II) at different airflow velocities

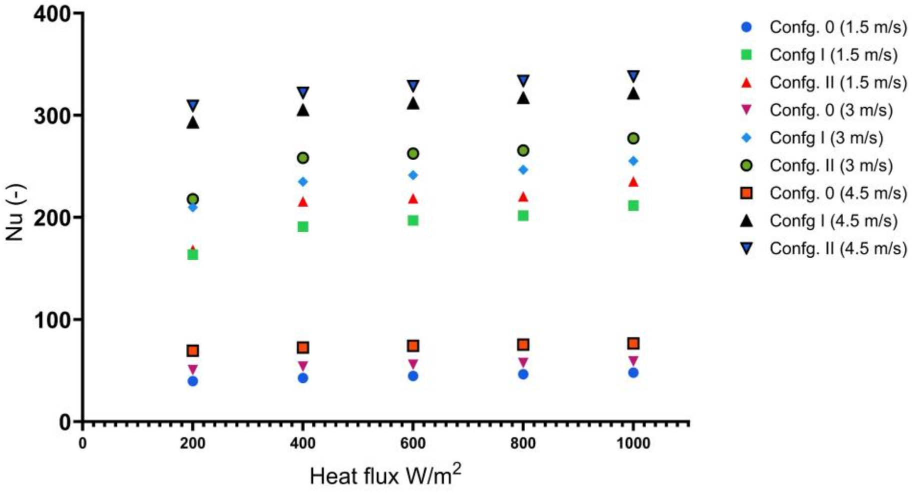

Figure 7. Variation of average Nusselt number with heat flux for smooth plate (Config. 0), triangular vortex generators (Config. I), and rectangular vortex generators (Config. II) at different airflow velocities

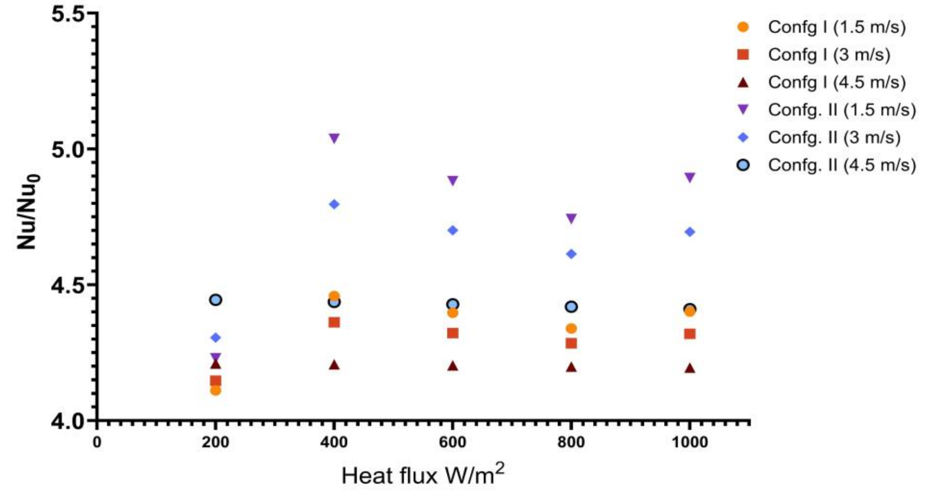

Figure 8. Normalized Nusselt number ratio (Nu/Nu_0) as a function of heat flux for triangular (Config. I) and rectangular (Config. II) vortex generator configurations compared to smooth plate baseline

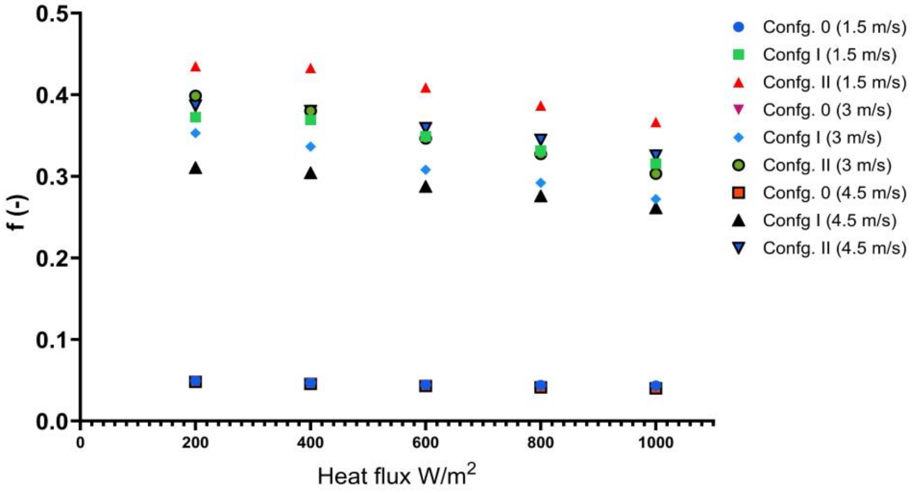

Figure 9. Variation of friction factor (f) with heat flux for different configurations and air velocities

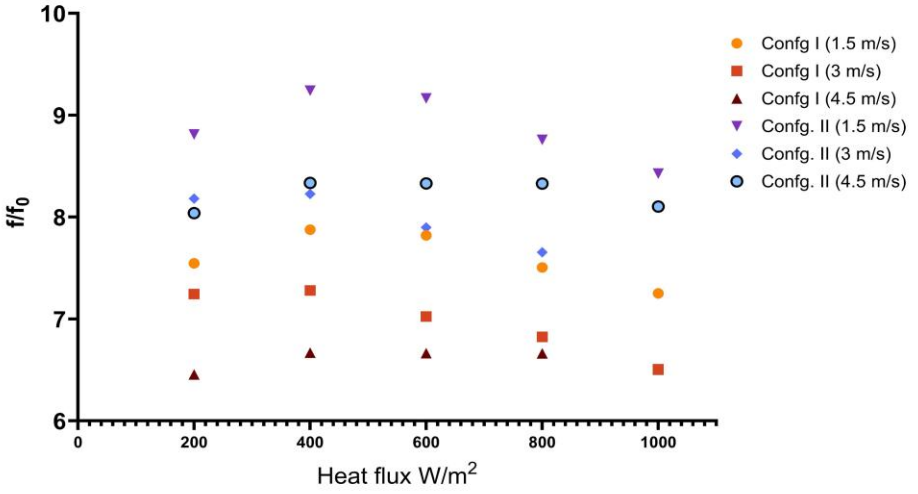

Figure 10. Normalized friction factor (f/f_0) comparison of vortex-generator configurations relative to smooth plate at various heat fluxes

Figure 10 shows the normalized friction factor (f/f_0) so that the penalty imposed by vortex generators can be more clearly seen in comparison with the smooth case. In all cases, f/f_0 remained in the 6–9 range, indicating that losses in pressure with vortex generators were an order of magnitude greater than the losses in the smooth plate. At low velocity (1.5 m/s), Config. II showed the highest penalty, with $f/f_0 \approx 9.0$, while Config. I gave $f/f_0 \approx 7.8$. The penalty decreased slightly at higher velocities, where Config. II dropped to $f/f_0 \approx 8.1$ at 4.5 m/s, and Config. I to $f/f_0 \approx 7.0$. This decreases in normalized values at the higher Reynolds numbers indicates that while vortex generators continue to add drag, the penalty becomes less severe with increasing velocity since the inertial effects outweigh the form drags.

The TPF is an important parameter since it encapsulates the twin effects of the augmentation of heat transfer and the penalty of enhanced frictional losses. As can be seen in Figure 11, the enhanced geometries (Config I - triangular wing and Config II - rectangular wing) show substantial gains over the smooth plate baseline (Config 0). Under a 200 W/m^2 heat flux, Config I resulted in a TPF of 1.7–1.95, whereas Config II resulted in ~.45-1.65. This translates to an increase in performance of almost 20–30% for Config I and 10-15% for Config II over the smooth channel. As the heat flux is increased to 1000 W/m^2, the TPF values for Config I and Config II increased further, reaching maxima of 2.0 and 1.75, respectively. This suggests that at increased thermal loading, vortex generators become better at sustaining augmentation of heat transfer in spite of the concomitant rise in frictional loss. The air velocity had a contributory effect. At 4.5 m/s, the Config I maintained the maximum TPF, more than 2.0, whereas the Config II stabilized at 1.75. As against, the smooth duct never reached a figure over unity (TPF 1), validating the superior thermo-hydraulic benefit of vortex generator configurations. Overall, the results highlight that incorporating vortex generators, especially triangular designs, can effectively double the thermal-hydraulic efficiency of FPSAHs under turbulent flow conditions.

Now to understand why the triangular wings outperform the rectangular wings at that regime we look into the details of the TPF curves at the lower air speed ($v = 1.5$ m/s, $Re \approx 9.5 \times 10^3$). For these moderate Reynolds numbers, the flow in the main duct is only weakly turbulent, and the recirculation regions created in behind the wings are left relatively coherent. The sharply-shaped peak of the triangular features encourages a quick yet uniform separation resulting in a nicely compact double pair of longitudinal vortex aligned with the bulk flow. Such coherent structures promote wall-normal mixing in the near-wall region while thinning the thermal boundary layer and do not create wake bubbles large enough to significantly increase pressure loss, resulting in a high increase of Nusselt number with respect to the pressure loss. In comparison, the orthogonal wings produce wider separated regions and higher form drag inducing a larger increase in friction factor for a given heat-transfer enhancement. As such, at $v = 1.5$ m/s the triangular configuration displays the highest TPF values, signifying a more advantageous balance between the heat-transfer augmentation and the pumping-power penalty, while the rectangular configuration becomes competitive predominantly at higher velocities at which inertial effects begin to prevail.

Figure 12 illustrates the parasitic friction design. From a practical design perspective, the higher friction observed in Figures 9–10 indicates that vortex generators require the fan to deliver more power when installed in the duct compared with a smooth duct configuration. The friction factor of the modified ducts is approximately six to nine times greater than that of the smooth duct for the same configurations, hence the pumping power is increased significantly. This penalty is however balanced with an unproportionately large increase in heat transfer, as the Nu increases up to four to five times, and the TPF reaches a value of ~2.0 for the triangular wings, and ~1.75 for the rectangular wings. The fan simply consumes more electric energy, in return for a much larger thermal yield on the collector. However, in the case of conventional small and medium flat-plate solar air heaters, the fan power only serves a small portion of the total energy balance while the additional useful heat could be great. Thus, for the range of operation studied in the present work, the implementation of vortex generators — and particularly the triangular-wing design — can be considered an energetically valid and practically sensible choice.

In order to understand the present results in valid context, a comparison of Nusselt number, friction factor and TPF values obtained are presented with the existing literature on solar air heater with vortex generators. The optimal combination was obtained with an enhancement ratio of Nusselt number and friction factor in respect of smooth duct: About 2–3 and a mass flow rate based thermo-hydraulic performance parameter close to 2.0 [23]. Bezbaruah et al. [20] and Pramod et al. [29] maximum thermo-hydraulic performance factors are also reported in the range of around 1.7–2.0. Nusselt number ratios of nearly 6 have been reported by Koolnapadol et al. [2], but accompanied by very large friction penalties, with friction factor ratios above 40 in some cases and less than 1.9 specific thermal performance best case. In the present study, the configuration with the rectangular-wing (Config. II) reaches Nu/Nu_0 of around 5 at f/f_0 ranging from 7 to 9 and maximum TPF of around 1.75, while the trapezoidal-wing configuration (Config. I) gives 4.1–4.5 Nu/Nu_0, f/f_0 between 7 and 8 and max 2.0 TPF. Such values show that the predicted inclined-wing designs provide a heat-transfer enhancement and thermo-hydraulic performance similar to that of state-of-the-art vortex-generator concepts, while clearly indicating the trade-off between the needed increase in Nusselt number and the inevitable increase in friction losses.

The characteristic temperature patterns in Figure 12 indicate the impact of vortex generator configurations on absorber plate cooling. In the smooth plate case (Config. 0), a relatively steady temperature gradient is shown, wherein higher wall temperatures are concentrated in the outlet region, 363 K. By adding vortex generators (Config. I and II), local mixing is increased, and convection heat transfer is enhanced so that sharp drops in the maximum surface temperature are observed. In Config. I, higher turbulence in the near of the mid-section generates more stretched-out cooling areas, therefore lowering the maximum temperature by about 20–25 K compared to the smooth plate case. In Config. II, the influence is increased further, as the reattachment zone of the flow generates long low-temperature streaks, therefore decreasing the maximum absorber plate surface temperature by about 30 K from Config. 0. This substantiates the finding that vortex generators can redistribute the load of heat, therefore reduce the thermal gradient and improve the absorber plate's thermal efficiency.

Figure 13 shows the contours of the velocity in the SAH duct at three various vortex generator configurations (Config. 0, I, and II) at an inlet velocity of 1.5 m/s. One can observe the marked differences in the internal flow patterns based on the used configuration. For Config. 0, the streamwise velocity is relatively steady, having minimum mixing and a distinct predominance of slow zones that cover most of the duct. This indicates that in the case of no vortex generator, the momentum transfer is insignificant, and the development of the boundary layer along the hot surface inhibits the enhancement of convection. Compared to it, Config. I generate strong acceleration bands at locations of the vortex generators, where the maximum velocities reach 1.8 m/s in localized areas. Due to the presence of the counter-rotating vortices, fluid entry is enhanced in the boundary layer, and mixing of the flow is increased, though there are some pockets of recirculation, suggesting moderate losses of pressure in this design. In Config. II, the strength of jet-like streams is even greater towards the outlet, with maximum values in excess of 1.85 m/s. In comparison with Config. I, the high-speed areas are longer and over a greater portion of the duct section, suggesting a better distribution of the entering flow. This increased mixing of the flow decreases stagnant areas and encourages greater convective transport at the heated walls. The penalty, however, is a greater pressure drop, in accordance with previous results in the form of friction factor ratios (Figure 10). Overall, the profiles confirm that Config. II offers the optimum flow redistribution, achieving 20–25% greater velocity gradients than Config. 0, which is a direct reflection of its superior heat transfer performance (Figures 6–8). Results once more supported the importance of secondary flow induction in improving solar air heater duct effectiveness, though it involves increased hydraulic losses.

The velocity fields in Figure 13. More direct measurements of the effects of the wings on the longitudinal vortex dynamics are also evident in 13. Every triangle, rectangle wing acts as a mini wing: flow stalls on one side, goes around the sharp leading edge, creating a pressure difference between the two surfaces. Together with local separation at the wing tips, this creates a pair of counter-rotating, streamwise vortices that are advected downstream along the absorber plate. These longitudinal vortices not only draw high-momentum fluid from the core region to the heated wall but also sweep low-momentum fluid away from the heated wall, thereby enhancing velocity gradients at near-wall area, thinning the thermal boundary layer, and strengthening the convective heat transfer. In the triangular arrangement, observed vortex cores are compact and aligned, providing significant boundary-layer disruption with moderate overall recirculation losses. In contrast, the prismatic wings produce wider recirculation zones and longer jet-like streaks that cause more prolonged regions of high speed, but also a larger form-drag cost. This difference is also the reason for the performance of the rectangular VGs providing some margin in peak Nusselt numbers, and the triangular VGs providing a better overall thermo-hydraulic compromise, which is quantified by TPF results of Figure 11.

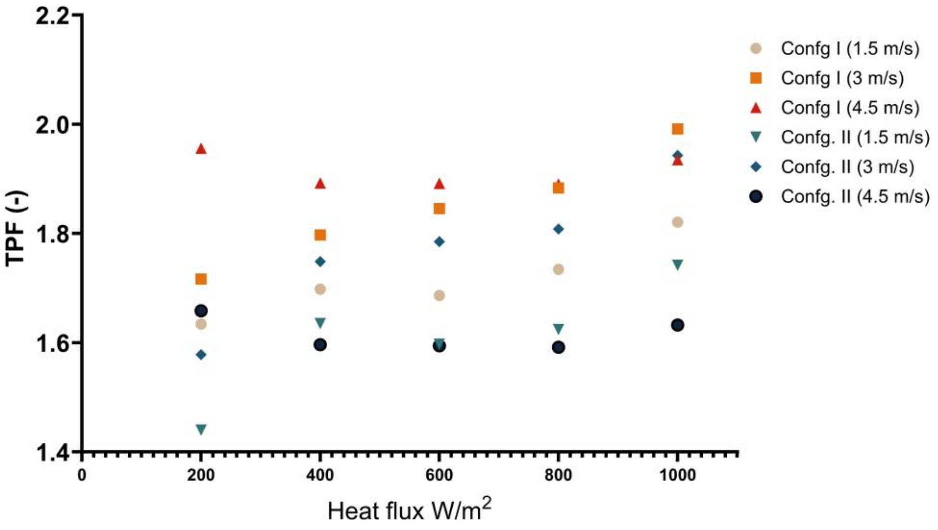

Figure 11. Variation of Thermal Performance Factor (TPF) with heat flux for different configurations and air velocities

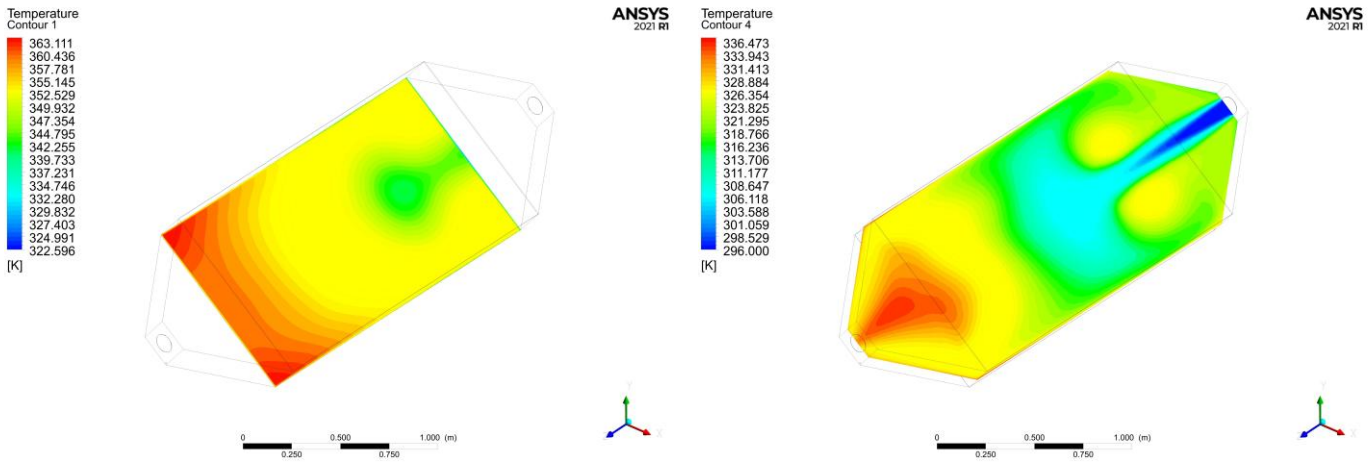

(a) Config. 0

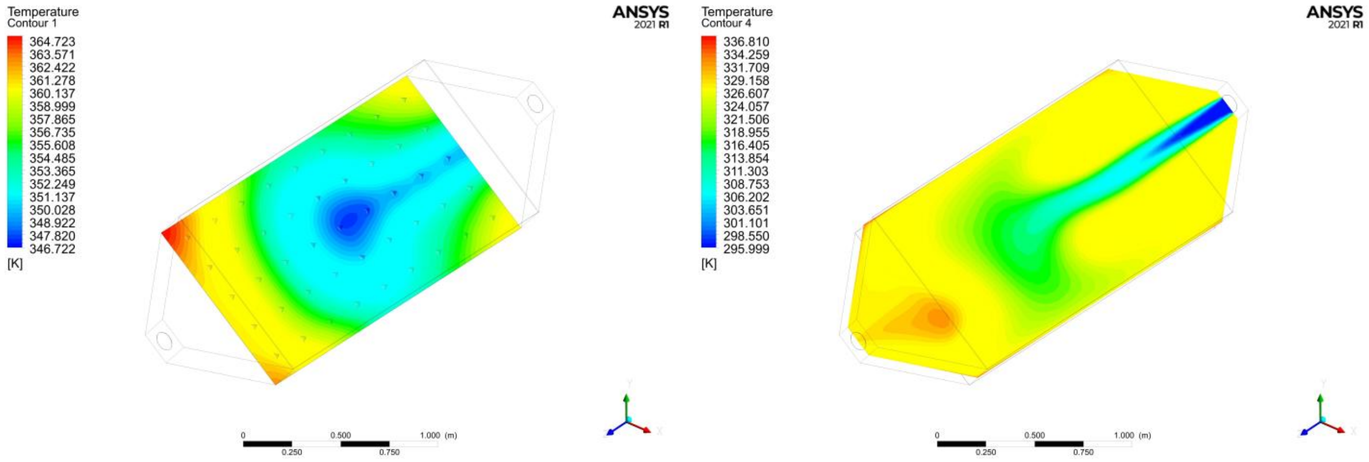

(b) Config. I

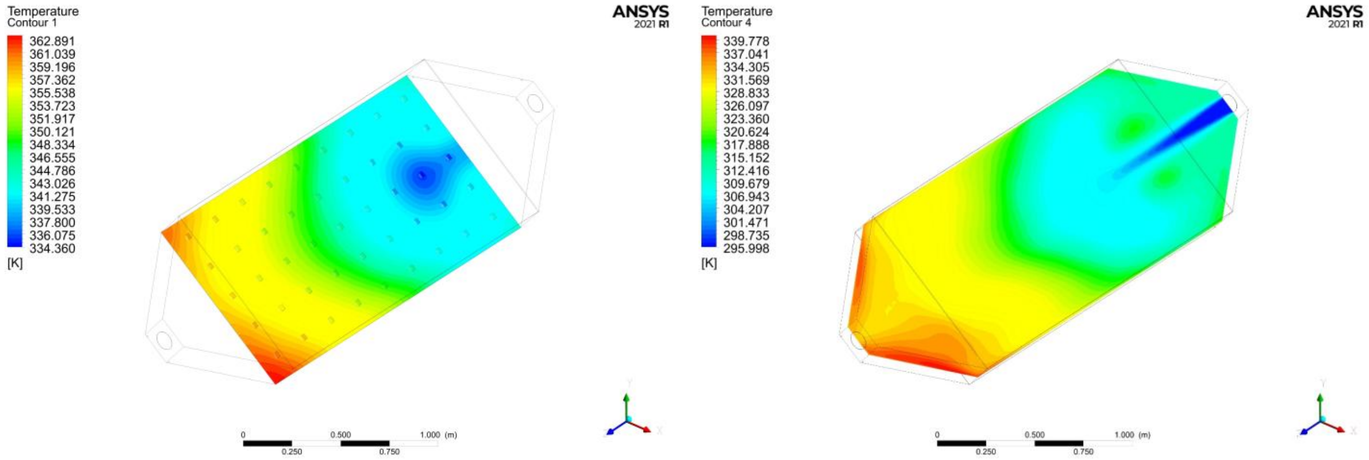

(c) Config. II

Figure 12. Temperature contours of the absorber plate at different vortex generator configurations: (a) smooth plate (Config. 0), (b) Config. I, and (c) Config. II

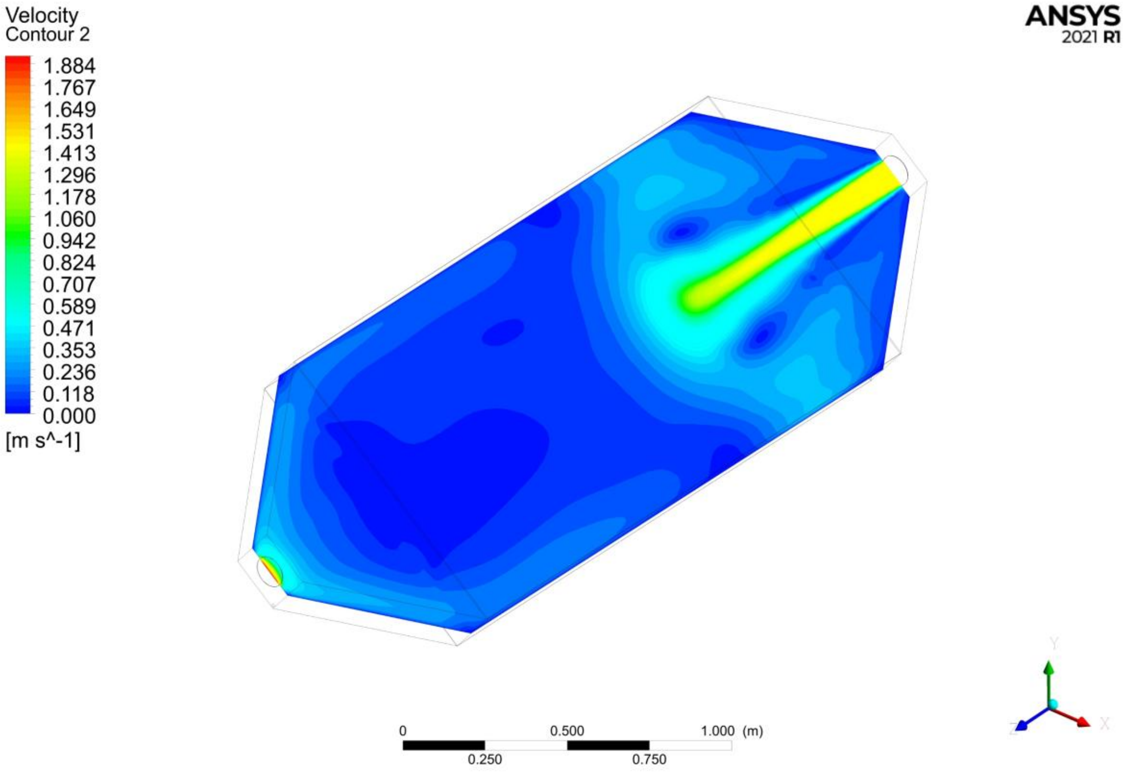

(a) Config 0

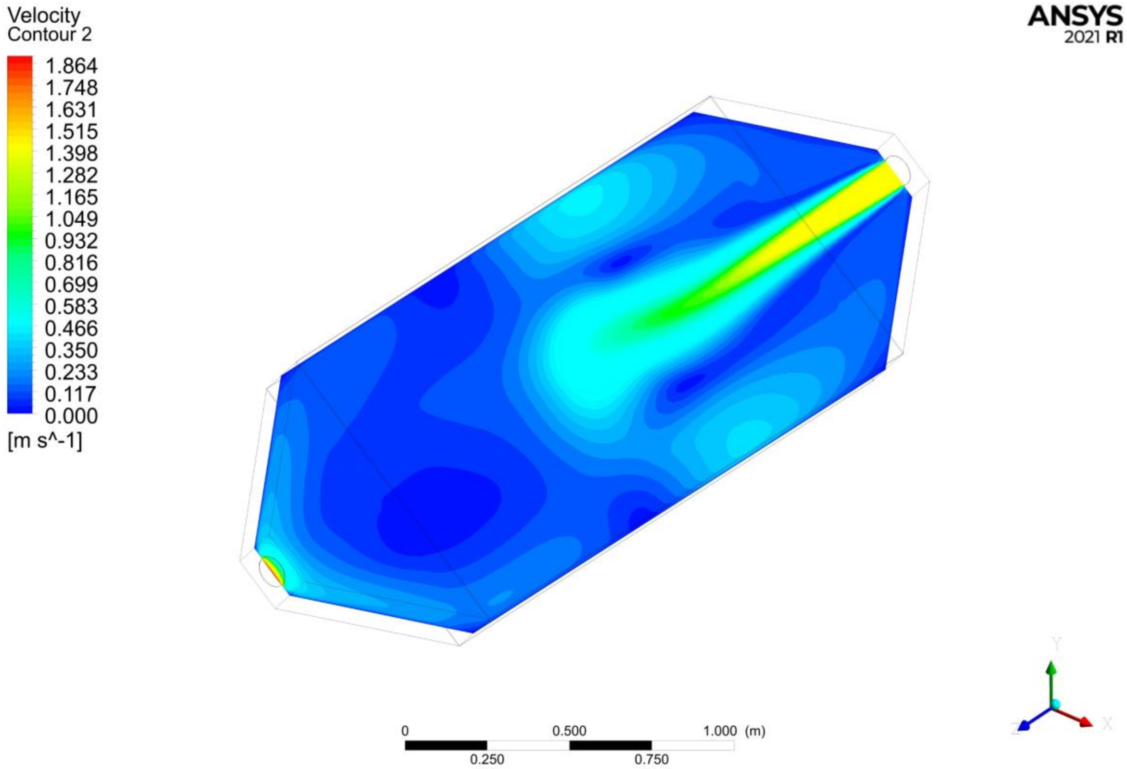

(b) Config. I

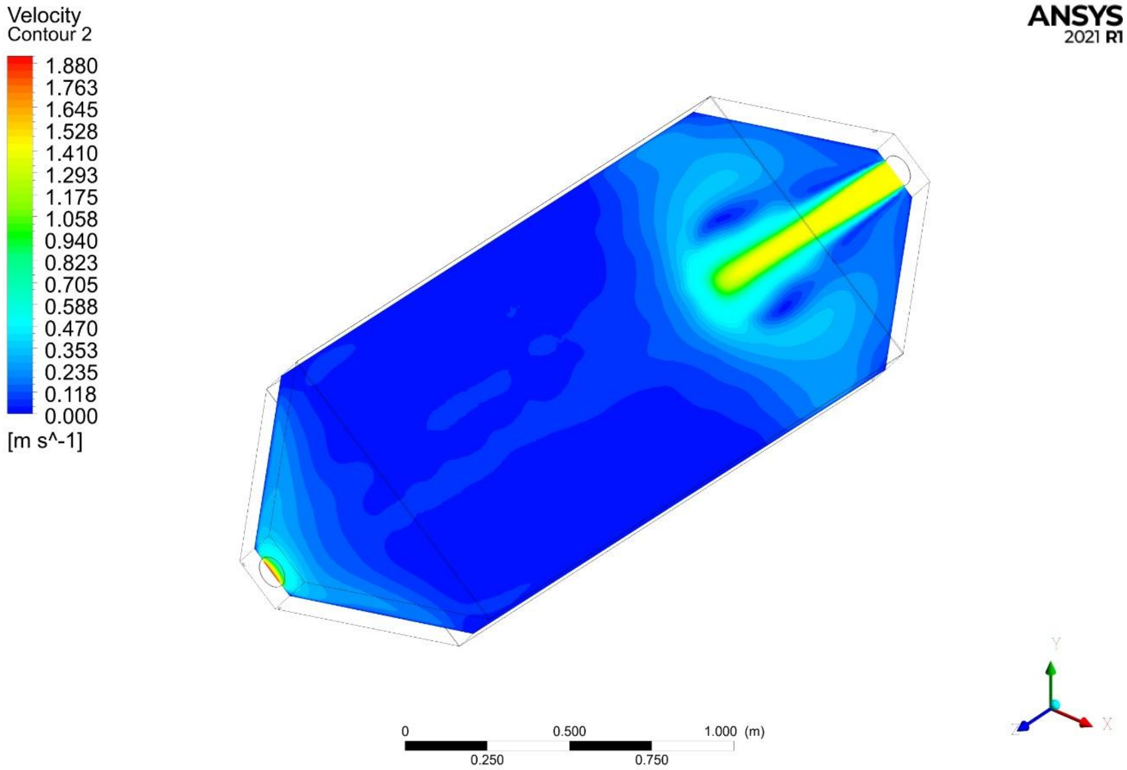

(c) Config. II

Figure 13. Velocity contours inside the SAH duct for different vortex generator configurations (Config. 0, Config. I, and Config. II) at an inlet velocity of 1.5 m/s

5. CONCLUSION

This study presented a CFD-based comparative analysis of three solar air heater configurations: smooth absorber plate (baseline), triangular wing vortex generators, and rectangular wing vortex generators, each inclined at 45°. The model was validated against established correlations and demonstrated strong agreement in terms of thermal and hydraulic predictions, thus providing confidence in the applied methodology.

The main results can be listed below:

- Outlet Temperature: Although the smooth duct had the largest outlet air temperatures because of the minimum turbulence, the triangular and the rectangle VG configurations provided higher heat transfer coefficients, verifying the fact that greater convective mixing outweighs the lower increase in bulk temperature.
- Heat Transfer Enhancement: Addition of VGs enhanced the Nusselt number by a maximum of 570% over the smooth plate. Rectangular VGs had the highest Nu values at all occasions, while triangular VGs provided slightly less but more stable augmentation over the entire velocity range.
- Hydraulic Penalty: Friction factors increased significantly, VG-equipped ducts reading values 6–9 times greater than those for the smooth plate. Rectangular wings produced the highest drag, while triangular wings provided a relatively lower penalty.
- TPF: Despite elevated friction losses, both VG configurations achieved TPF >1.0, validating their overall advantage. Triangular VGs demonstrated the best balance, attaining TPF 2.0 at higher heat fluxes and velocities, compared to 1.75 for rectangular VGs.

In conclusion, vortex generators significantly enhance the thermo-hydraulic efficiency of flat plate SAHs. Triangular wing VGs offer the optimal configuration, delivering nearly double the thermal-hydraulic performance of the smooth duct. This suggests that triangular VGs are the most promising passive design for practical solar thermal applications, where maximizing energy gain while minimizing pumping power remains critical.

REFERENCES

[1] Prakash, R., Kamatchi, R. (2024). Natural convective solar dryer powered by stepped fin plate integrated trough array solar air heater for agricultural produce preservations. Solar Energy, 271: 112415. https://doi.org/10.1016/j.solener.2024.112415

[2] Koolnapadol, N., Promvonge, P., Skullong, S. (2020). Performance evaluation of solar receiver heat exchanger with rectangular-wing vortex generators. International Journal of Mechanical Engineering and Robotics Research, 9(1): 130-135. https://doi.org/10.18178/ijmerr.9.1.130-135

[3] Pardeshi, P.S., Boulic, M., van Heerden, A.H., Phipps, R., Cunningham, C.W. (2024). Review of the thermal efficiency of a tube-type solar air heaters. Renewable and Sustainable Energy Reviews, 199: 114509. https://doi.org/10.1016/j.rser.2024.114509

[4] Dezan, D.J., Rocha, A.D., Ferreira, W.G. (2020). Parametric sensitivity analysis and optimisation of a solar air heater with multiple rows of longitudinal vortex generators. Applied Energy, 263: 114556. https://doi.org/10.1016/j.apenergy.2020.114556

[5] El-Fakharany, M.K., Abo-Samra, A.E.A., Abdelmaqsoud, A.M., Marzouk, S.A. (2024). Enhanced performance assessment of an integrated evacuated tube and flat plate collector solar air heater with thermal storage material. Applied Thermal Engineering, 243: 122653. https://doi.org/10.1016/j.applthermaleng.2024.122653

[6] Kabeel, A.E., Hamed, M.H., Omara, Z.M., Kandeal, A.W. (2017). Solar air heaters: Design configurations, improvement methods and applications–A detailed review. Renewable and Sustainable Energy Reviews, 70: 1189-1206. https://doi.org/10.1016/j.rser.2016.12.021

[7] Bhuvad, S.S., Azad, R., Lanjewar, A. (2022). Thermal performance analysis of apex-up discrete arc ribs solar air heater-an experimental study. Renewable Energy, 185: 403-415. https://doi.org/10.1016/j.renene.2021.12.037

[8] Chamarthi, S., Singh, S. (2021). A comprehensive review of experimental investigation procedures and thermal performance enhancement techniques of solar air heaters. International Journal of Energy Research, 45(4): 5098-5164. https://doi.org/10.1002/er.6255

[9] Chamoli, S., Lu, R., Xu, D., Yu, P. (2018). Thermal performance improvement of a solar air heater fitted with winglet vortex generators. Solar Energy, 159: 966-983. https://doi.org/10.1016/j.solener.2017.11.046

[10] Alrashidi, A., Altohamy, A.A., Abdelrahman, M.A., Elsemary, I.M. (2024). Energy and exergy experimental analysis for innovative finned plate solar air heater. Case Studies in Thermal Engineering, 59: 104570. https://doi.org/10.1016/j.csite.2024.104570

[11] Sharma, A., Thakur, S., Dhiman, P. (2023). An integrated active-passive solution for strengthening the functionality of a solar air heater. Energy Sources, Part A: Recovery, Utilization, and Environmental Effects, 45(1): 1-17. https://doi.org/10.1080/15567036.2022.2161675

[12] Tanda, G. (2011). Performance of solar air heater ducts with different types of ribs on the absorber plate. Energy, 36(11): 6651-6660. https://doi.org/10.1016/j.energy.2011.08.043

[13] Matsunaga, J., Kikuta, K., Hirakawa, H., Mizuno, K., Tajima, M., Hayashi, M., Fukushima, A. (2021). An assessment of heating load reduction by a solar air heater in a residential passive ventilation system. Energies, 14(22): 7651. https://doi.org/10.3390/en14227651

[14] Nidhul, K., Yadav, A.K., Anish, S., Kumar, S. (2021). Critical review of ribbed solar air heater and performance evaluation of various V-rib configuration. Renewable and Sustainable Energy Reviews, 142: 110871. https://doi.org/10.1016/j.rser.2021.110871

[15] Nassab, S.G., Sheikhnejad, Y., Nia, M.F. (2022). Novel design of natural solar air heat for higher thermal performance utilizing porous vortex generator. Thermal Science and Engineering Progress, 33: 101385. https://doi.org/10.1016/j.tsep.2022.101385

[16] Zhao, Z., Luo, L., Qiu, D., Wang, Z., Sundén, B. (2021). On the solar air heater thermal enhancement and flow topology using differently shaped ribs combined with delta-winglet vortex generators. Energy, 224: 119944. https://doi.org/10.1016/j.energy.2021.119944

[17] Chaurasia, S., Goel, V., Debbarma, A. (2023). Impact of hybrid roughness geometry on heat transfer augmentation in solar air heater: A review. Solar Energy, 255: 435-459. https://doi.org/10.1016/j.solener.2023.02.052

[18] Pinto, R.V., Duarte, R.M.D., Ferreira, W.G., Dezan, D.J. (2025). Thermal–hydraulic performance evaluation of solar air heaters containing longitudinal vortex generators: Review and meta-analysis. Journal of the Brazilian Society of Mechanical Sciences and Engineering, 47(4): 160. https://doi.org/10.1007/s40430-025-05474-4

[19] Charoensin-O-larn, R., Lertnuwat, B. (2025). Effect of upwind and downwind directions of right-trapezoidal winglet-vortex-generators in a solar-air-heater. Heat Transfer Engineering, 46(12): 989-1006. https://doi.org/10.1080/01457632.2024.2362537

[20] Bezbaruah, P.J., Das, R.S., Sarkar, B.K. (2021). Experimental and numerical analysis of solar air heater accoutered with modified conical vortex generators in a staggered fashion. Renewable Energy, 180: 109-131. https://doi.org/10.1016/j.renene.2021.08.046

[21] Lertnuwat, B. (2024). Effect of the number and placement of punched holes in rectangular winglet vortex generators on solar air heater performance. Energy Conversion and Management: X, 24: 100714. https://doi.org/10.1016/j.ecmx.2024.100714

[22] Hu, J., Zhang, Y., Xie, S., Xiao, Y. (2024). Thermo-hydraulic performance of solar air heater with built-in one-eighth sphere vortex generators. Applied Thermal Engineering, 245: 122837. https://doi.org/10.1016/j.applthermaleng.2024.122837

[23] Duarte, R.M., Salviano, L.O., Ferreira, W.G., Dezan, D.J. (2023). Numerical investigation of heat transfer enhancement by using louvered-winglet vortex generators mounted in a solar air heater channel-type. Journal of Thermal Analysis and Calorimetry, 148(24): 14183-14204. https://doi.org/10.1007/s10973-023-12599-y

[24] Van Hap, N., Nhan, P.T., Hien, H.P., Phu, N.M. (2023). Thermohydraulic performance augmentation in a solar air heater using a perforated circular segment vortex generator. Environmental Science and Pollution Research, 30(24): 65338-65350. https://doi.org/10.1007/s11356-023-26987-2

[25] Lertnuwat, B. (2022). The effect of the hole position on trapezoidal winglet vortex generators in a rectangular-duct-type solar air heater. Journal of Mechanical Science and Technology, 36(12): 6345-6354. https://doi.org/10.1007/s12206-022-1146-y

[26] Sari, A., Sadi, M., Shafiei Sabet, G., Mohammadiun, M., Mohammadiun, H. (2021). Experimental analysis and exergetic assessment of the solar air collector with delta winglet vortex generators and baffles. Journal of Thermal Analysis and Calorimetry, 145(3): 867-885. https://doi.org/10.1007/s10973-020-10298-6

[27] Promvonge, P., Promthaisong, P., Skullong, S. (2021). Numerical heat transfer in a solar air heater duct with punched delta-winglet vortex generators. Case Studies in Thermal Engineering, 26: 101088. https://doi.org/10.1016/j.csite.2021.101088

[28] Alnakeeb, M.A., Hassan, M.A., Teamah, M.A. (2024). Thermal performance analysis of corrugated plate solar air heater integrated with vortex generator. Alexandria Engineering Journal, 97: 241-255. https://doi.org/10.1016/j.aej.2024.04.019

[29] Pramod, G.K., Madhwesh, N., Arunachala, U.C., Manjunath, M.S. (2024). Thermohydraulic performance augmentation of triangular duct solar air heater using semi-conical vortex generators: Numerical and experimental study. Heat Transfer, 53(6): 3021-3053. https://doi.org/10.1002/htj.23077